

## Photonic band gap materials comprising positive-phase-velocity and negative-phase-velocity layers in waveguides

Álvaro Gómez<sup>a\*</sup>, María L. Martínez Ricci<sup>b</sup>, Ricardo A. Depine<sup>b</sup> and Akhlesh Lakhtakia<sup>c</sup>

<sup>a</sup>Grupo de Electromagnetismo Computacional, Departamento de Electricidad y Electrónica, Universidad de Valladolid, Paseo Prado de la Magdalena s/n, 47011 Valladolid, Spain; <sup>b</sup>Grupo de Electromagnetismo Aplicado, Departamento de Física, Facultad de Ciencias Exactas y Naturales, Universidad de Buenos Aires, Ciudad Universitaria, Pabellón 1, 1428 Buenos Aires, Argentina; <sup>c</sup>NanoMM–Nanoengineered Metamaterials Group, Department of Engineering Science and Mechanics, Pennsylvania State University, University Park, PA 16802-6812, USA

(Received 13 May 2009; final version received 21 August 2009)

We have analyzed electromagnetic wave propagation in photonic bandgap (PBG) structures comprising alternating layers of isotropic dielectric-magnetic materials with positive phase velocity and negative phase velocity, implemented in different waveguides of uniform cross-section (parallel-plate, rectangular, circular, and coaxial) and perfectly conducting walls. The structures could be either ideal (i.e. of infinite extent along the waveguide axis) or real (i.e. terminated at both ends with homogeneously filled waveguide sections). The spectral locations of the band gaps do not directly depend on the cross-sectional shape and dimensions, but on the cut-off parameter instead, for ideal structures. The band gaps of an ideal structure are located in spectral regions where the reflectance of the corresponding real structure is large. The real structures show four types of band gaps, only one type of which is due to the periodically repetitive constitution of the PBG structure; the remaining three types are not of the Bragg type.

**Keywords:** circular waveguides; coaxial waveguides; gap map; negative phase velocity; parallel-plate waveguide; photonic band gap; rectangular waveguide

### 1. Introduction

Periodic arrangements of two or more dissimilar materials are called photonic band gap (PBG) structures. These structures can manipulate the flow of light [1–3], and are expected to lead to commercially important devices [4–6]. PBG structures have frequency-selective response properties: there are frequency-ranges (called photonic band gaps or stopbands) in which propagation is forbidden, and there are frequency ranges (called passbands) wherein transmission is allowed. A periodic stack of layers or sheets, called a periodic multilayer, is the simplest PBG structure. Such 1-D PBG structures are mainly used as distributed Bragg reflectors [7–9].

The possible incorporation of negatively refracting materials in PBG structures is an attractive idea. Isotropic, negatively refracting materials had been hypothesized for about a century, most memorably by Veselago in 1967 [10], but were not realized until 2001. Much theoretical and experimental work has been reported since then [11–13]. In their simplest form, these passive materials are isotropic, dielectric-magnetic substances whose permittivity and

permeability obey a certain condition in a particular frequency range [14]. As a result, the phase velocity and the time-averaged Poynting vector of a plane wave have opposite directions; therefore, these materials are also called negative-phase-velocity (NPV) materials [15]. By analogy, materials that do not satisfy the NPV condition are called positive-phase-velocity (PPV) materials, because the phase velocity and the time-averaged Poynting vector then are co-parallel. Most notably, NPV materials are said to hold promise for almost perfect, flat lenses [16–22].

The study of electromagnetic propagation through 1-D PBG structures containing NPV materials has shown the existence of new band gaps that arise due to the presence of the NPV materials. Alternating PPV-NPV multilayers exhibit the zero-index band gap [17,18] when the volumetrically averaged refractive index of the unit cell equals zero. The resonance behavior of the NPV constitutive parameters gives rise to the  $\mu$ -zero and  $\varepsilon$ -zero band gaps [23,24]. In contrast to the usual Bragg PBGs, these two new types of band gaps are invariant to scale-change and robust against disorder, properties that could encourage the

---

\*Corresponding author. Email: [alomezgom@yahoo.es](mailto:alomezgom@yahoo.es)

fabrication of novel devices. NPV materials have been widely developed in the microwave and millimeter regimes (the optical regime has recently been reached [25–27]), in which regimes' the finite transverse dimensions play an important role [9]. A waveguide completely filled with an NPV material has already been found to exhibit new and unusual properties such as zero flux energy for the design of an optical trap [28] or absence of a fundamental mode [29]. These studies had earlier led us to consider the electromagnetic response of a periodic multilayer inserted in a parallel-plate waveguide, with a unit cell comprising a PPV layer and an NPV layer, and the direction of propagation being generally oblique to the stratification direction [30]. Both walls of the waveguide were taken to be perfectly conducting. The number of unit cells could be either infinite or finite (as for real structures). Comparison of guided wave propagation (a) in the parallel-plate waveguide and (b) in the stratification direction as well as obliquely in the same 1-D PBG structure but of infinite transverse extent assisted in the explanation of several band gap features and reflectance peaks, particularly those associated with non-Bragg gaps obtained for (a).

Continuing with the same theme, and in order to analyze the influence of the cross-sectional shape of the waveguide, we considered the characteristics of propagation in waveguides of different cross-sectional shapes filled either completely or partially with a 1-D PBG structure whose unit cell comprises a PPV layer and an NPV layer. If the chosen 1-D PBG structure is of finite thickness, then both ends of the waveguide are supposed to be filled with a PPV material. The walls of the waveguide are perfectly conducting.

To acquire a full theoretical understanding, in Section 2 of this paper we provide a brief introduction to every item involved in our calculations, from electromagnetic propagation in waveguides of different cross-sections to bilayer dispersion relations including the two numerical techniques used to determine the response of real multilayer structures. Section 3 presents a thorough analysis of the influences that the cross-section geometries and dimensions have on the electromagnetic responses of the studied systems. Finally, Section 4 presents a summary and conclusions of the results obtained in the present work.

## 2. Basic theory

### 2.1. Ideal PBG structure

Let us consider an ideal PBG multilayer comprising PPV and NPV layers implemented inside a waveguide with arbitrary closed cross-sectional shape and perfectly conducting walls, as illustrated in Figure 1. We chose an orthogonal curvilinear cylindrical

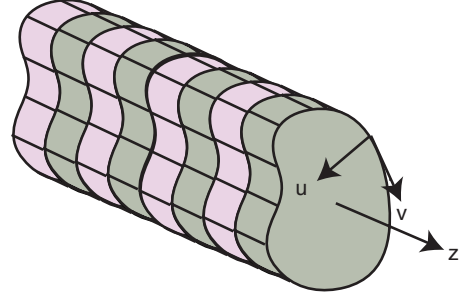


Figure 1. Schematic of a waveguide filled completely by a PBG multilayer of period  $d$ . (The color version of this figure is included in the online version of the journal.)

coordinate system  $(u, v, z)$  with unit vectors  $\mathbf{u}$ ,  $\mathbf{v}$  and  $\mathbf{z}$  [31]. The PBG multilayer has a spatial period  $d = d_1 + d_2$  along the  $z$  axis; hence, the relative permittivity  $\varepsilon(z)$  and relative permeability  $\mu(z)$  obey the relations  $\varepsilon(z + d) = \varepsilon(z)$  and  $\mu(z + d) = \mu(z)$ , with the reference unit cell  $d_1 \geq z \geq -d_2$  characterized by

$$\varepsilon(z) = \begin{cases} \varepsilon_1 & \text{if } 0 \leq z \leq d_1, \\ \varepsilon_2 & \text{if } -d_2 \leq z \leq 0, \end{cases} \quad (1)$$

$$\mu(z) = \begin{cases} \mu_1 & \text{if } 0 \leq z \leq d_1, \\ \mu_2 & \text{if } -d_2 \leq z \leq 0. \end{cases} \quad (2)$$

Propagation was taken to occur in the stratification direction (i.e. parallel to the  $z$  axis). With the assumption of an  $\exp(-i\omega t)$  time-dependence, the electromagnetic field phasors,  $\mathbf{E}(u, v, z)$  and  $\mathbf{H}(u, v, z)$ , inside the waveguide are given as solutions of the vector Helmholtz equation

$$\left[ \nabla^2 + \frac{\omega^2}{c^2} \varepsilon(z) \mu(z) \right] \begin{Bmatrix} E(u, v, z) \\ H(u, v, z) \end{Bmatrix} = 0, \quad (3)$$

where  $c$  is the speed of light in free space. Independently of the cross-sectional shape, these fields can be expressed as an infinite superposition of modal fields, each of which is a solution of (3) [32]. Moreover, as the product  $\varepsilon(z)\mu(z)$  is piecewise uniform, each modal field inside the  $j$ th layer,  $j \in \{1, 2\}$ , of the unit cell can be expressed in terms of a superposition of forward and backward waves with  $z$  dependence given by  $\exp(\pm\beta_{nm}^{(j)}z)$ , where the mode indexes  $n$  and  $m$  are natural numbers.

As described in detail by Jackson [32], modal fields can be separated into transverse (perpendicular to the  $z$  axis) and longitudinal (parallel to the  $z$  axis) components. The longitudinal components are found by solving the scalar Helmholtz equation

$$[\nabla_t^2 + \Gamma_{nm}^2] \psi_{nm}(u, v) = 0, \quad (4)$$

where  $\nabla_t^2 \equiv \nabla^2 - \partial^2/\partial z^2$  and  $\psi_{nm}(u, v)$  is the longitudinal component for each  $nm$  mode of the magnetic (electric) field in the  $TE^z$  ( $TM^z$ ) polarization state. The cut-off wavenumber  $\Gamma_{nm}$  emerges from the imposition of the boundary conditions on the perfectly conducting walls of the waveguide, and thus depends only on the cross-sectional shape and size. Accordingly, the propagation constant

$$\beta_{nm}^{(j)} = \sqrt{\frac{\omega^2}{c^2} \varepsilon_j \mu_j - \Gamma_{nm}^2}, \quad j = 1, 2 \quad (5)$$

has to be defined for a mode with the  $(n, m)$  index in the  $j$ th layer.

## 2.2. Chosen cross-sectional shapes

So far, the analysis presented holds for a cylindrical waveguide with an arbitrary cross-sectional shape. Therefore, it covers PBG multilayers with infinite transverse dimensions [33], as well as PBG multilayers implemented in parallel-plate [30,34], rectangular [35], and circular [36] waveguides. Even coaxial waveguides lie within the scope of the presented analysis. We chose to study the following types of waveguides.

- *Parallel-plate waveguide.* The walls are the planes  $y = \pm h/2$ . Then the index  $m$  becomes meaningless, and both  $TE^z$  and  $TM^z$  modes have the same cut-off wavenumber

$$\Gamma_n = \sqrt{\frac{n\pi}{h}}, \quad n = 1, 2, 3, \dots \quad (6)$$

Also allowed is the  $TM^z$  mode with  $n=0$ , which is the  $TEM$  mode. As this mode is insensitive to the presence of the waveguide walls, we excluded it from our analysis.

- *Rectangular waveguide.* The walls are formed by the planes  $x = \pm a/2$  and  $y = \pm b/2$ . Again, the  $TE^z$  and  $TM^z$  modes have the same cut-off wavenumber

$$\Gamma_{nm} = \sqrt{\left(\frac{n\pi}{a}\right)^2 + \left(\frac{m\pi}{b}\right)^2}. \quad (7)$$

The indexes  $n, m=0, 1, 2, \dots$  (but with  $n=m=0$  disallowed) for  $TE^z$  modes and  $n, m=1, 2, 3, \dots$  for  $TM^z$  modes.

- *Circular waveguide.* The wall is a tube of radius  $a$ . The cut-off wavenumbers for  $TE^z$  and  $TM^z$  modes are different.

- $TE^z$  modes

$$\Gamma_{nm} = \frac{\chi'_{nm}}{a} \quad (8)$$

where  $\chi'_{nm}$  is the  $m$ th zero of the first derivative of the Bessel function of the first kind and order  $n$ , i.e.  $dJ_n(\chi')/d\chi' = 0$ ,  $n=0, 1, 2, \dots$

- $TM^z$  modes

$$\Gamma_{nm} = \frac{\chi_{nm}}{a} \quad (9)$$

where  $\chi_{nm}$  is the  $m$ th zero of the Bessel function of first kind and order  $n$ , i.e.,  $J_n(\chi) = 0$ ,  $n=0, 1, 2, \dots$

- *Coaxial waveguide.* The walls are tubes of radii  $r_{in}$  and  $r_{ext}$ . The cut-off wavenumbers for  $TE^z$  and  $TM^z$  modes are different and can be found by solving the following characteristic equations:

- $TE^z$  modes

$$J'_n(\Gamma_{nm}r_{in})Y'_n(\Gamma_{nm}r_{ext}) - J'_n(\Gamma_{nm}r_{ext})Y'_n(\Gamma_{nm}r_{in}) = 0. \quad (10)$$

- $TM^z$  modes

$$J_n(\Gamma_{nm}r_{in})Y_n(\Gamma_{nm}r_{ext}) - J_n(\Gamma_{nm}r_{ext})Y_n(\Gamma_{nm}r_{in}) = 0. \quad (11)$$

The function  $Y_n$  is the Bessel function of the second kind and order  $n$ , and the prime on a Bessel function indicates the first derivative with respect to the argument.

## 2.3. Dispersion relation

In order to obtain the multilayer dispersion relation for propagation of  $TE^z$  and  $TM^z$  modes, only the reference unit cell  $d_1 \geq z \geq -d_2$  needs to be considered. Boundary conditions have to be enforced on the  $u$ -directed and  $v$ -directed components of the electric and the magnetic fields across the bimaterial interface  $z = 0$ , and the Floquet-Bloch theorem [33] has to be implemented on the planes  $z = d_1$  and  $z = -d_2$ . Furthermore, the orthogonalities of the functions  $\psi_{nm}(u, v)$  have to be exploited. For each mode with index  $(n, m)$ , the dispersion relation

$$L_{nm} = \cos(Kd) = \cos(\beta_{nm}^{(1)}d_1) \cos(\beta_{nm}^{(2)}d_2) - \frac{1}{2} \left( \frac{\sigma_2 \beta_{nm}^{(1)}}{\sigma_1 \beta_{nm}^{(2)}} + \frac{\sigma_1 \beta_{nm}^{(2)}}{\sigma_2 \beta_{nm}^{(1)}} \right) \sin(\beta_{nm}^{(1)}d_1) \sin(\beta_{nm}^{(2)}d_2), \quad (12)$$

is obtained, where  $K$  is the Bloch wavenumber and

$$\sigma_j = \begin{cases} \mu_j & \text{for } TE^z \text{ modes,} \\ \varepsilon_j & \text{for } TM^z \text{ modes.} \end{cases} \quad (13)$$

The dispersion relation (2) rules the electromagnetic characteristics of the PBG multilayer implemented in a waveguide. As the dispersion relations involves the propagation constants  $\beta_{nm}^{(j)}$ ,  $j \in \{1, 2\}$ , defined in Equation (5), the cross-sectional geometry of the waveguide must influence the spectral locations of the passbands and the stopbands.

The passbands and stopbands can be distinguished from each other analytically as follows. If dissipation in both materials in the unit cell is small enough to be ignored, the function  $L_{nm} = \cos(Kd)$  is then real-valued for all modes. The frequency ranges for which the condition  $|L_{nm}| \leq 1$  is satisfied are associated with real-valued Bloch wavenumbers and therefore are passbands. Stopbands are associated with the satisfaction of the condition  $|L_{nm}| > 1$  for which the Bloch wavenumbers must be complex-valued.

In a periodic multilayer comprising NPV and PPV constituent materials, the following different types of photonic band gaps (stopbands) can be distinguished [23]:

- Bragg band gaps:
  - these band gaps are characteristic of periodic structures independently of the direction of the phase velocity. They appear under the following conditions:

$$\begin{aligned} \beta_{nm}^{(1)}d_1 + \beta_{nm}^{(2)}d_2 &= p\pi, \quad p = \pm 1, \pm 2, \dots, \\ \sigma_2\beta_{nm}^{(1)} &\neq \sigma_1\beta_{nm}^{(2)}, \\ \beta_{nm}^{(1)}d_1 &\neq q\pi, \quad q = \pm 1, \pm 2, \dots \end{aligned} \quad (14)$$

- Band gaps of other types:
  - $\bar{n} = 0$  band gap: This band gap appears when the condition for zero (volume) averaged refractive index is met, which occurs when the following conditions are simultaneously satisfied:

$$\begin{cases} \sigma_2\beta_{nm}^{(1)} \neq \sigma_1\beta_{nm}^{(2)}, \\ \beta_{nm}^{(1)}d_1 + \beta_{nm}^{(2)}d_2 = 0. \end{cases} \quad (15)$$

- $\mu$ -zero and  $\varepsilon$ -zero band gaps: these types of band gaps appear in frequency ranges wherein one of the two constituent materials of the unit cell has a zero refractive index [23,24]. When one of the two relative permittivities (permittivities) equals zero but neither of the relative permeabilities (permeabilities) is null-valued, a band gap may occur for  $TE^z$  ( $TM^z$ ) modes.

## 2.4. Real PBG structure

A real PBG multilayer must have a finite thickness and must contain a finite number of unit cells. Hence, the Floquet-Bloch theorem becomes inapplicable. Furthermore, a real PBG multilayer implemented in a waveguide must be coupled to input and output waveguide sections. We chose the input and output sections to have the same cross-section as the waveguide section containing the real PBG multilayer. We also chose the input and output sections to be unfilled.

In order to determine the electromagnetic characteristics of this type of structure, we used two different procedures. The first procedure is based on the Abelés method [37] and involves the use of Chebyshev polynomials [38]. The second procedure is formulated in terms of an overall scattering matrix [39].

### 2.4.1. Abelés–Chebyshev procedure (ACP)

In this procedure, boundary conditions are enforced across every interface of two layers. This allows us to relate field amplitudes in one layer with those in an adjacent layer by means of a  $2 \times 2$  transfer matrix  $\mathbf{P}$ , which thus characterizes the unit cell. Provided the dissipation is small enough to be ignored,  $\det(\mathbf{P}) = 1$  and  $\text{tr}(\mathbf{P})$  is real-valued. If there are  $N$  unit cells, the matrix  $\mathbf{P}^N$  characterizes them all together. After exploiting the Cayley–Hamilton theorem,  $\mathbf{P}^N$  can be expressed as a linear combination of  $\mathbf{P}$  and the  $2 \times 2$  identity matrix  $\mathbf{I}$  [38]. The coefficients of this linear combination are  $U_{N-1}(L_{nm})$  and  $U_{N-2}(L_{nm})$ , which are Chebyshev polynomials of order  $N-1$  and  $N-2$ , where  $L_{nm}$  is defined in Equation (12).

Taking advantage of this formalism, the reflectance and transmittance of a real PBG structure for the  $(n, m)$  index can be computed as

$$R_{nm} = \frac{|\zeta_{nm}|^2 U_{N-1}(L_{nm})}{1 + |\zeta_{nm}|^2 U_{N-1}(L_{nm})}, \quad (16)$$

$$T_{nm} = \frac{1}{1 + |\zeta_{nm}|^2 U_{N-1}(L_{nm})}, \quad (17)$$

with

$$\zeta_{nm} = \frac{i}{2} \left( \frac{\beta_{nm}^{(1)}\sigma_2}{\beta_{nm}^{(2)}\sigma_1} + \frac{\beta_{nm}^{(2)}\sigma_1}{\beta_{nm}^{(1)}\sigma_2} \right) \sin(\beta_{nm}^{(2)}d_2).$$

### 2.4.2. Scattering-matrix procedure (SMP)

In this procedure, every interface of two layers is treated as the junction of two semi-infinite waveguides filled homogeneously with different materials, in such



a way that the usual  $TE^z$  and  $TM^z$  modes are matched at the junction to produce a generalized scattering matrix (GSM) [39]. Since no internal discontinuity is present in the transverse plane, each mode individually satisfies the boundary conditions at every bimaterial interface along the  $z$ -axis. Consequently, a GSM for a specific mode characterized by the  $(n, m)$  index can be formulated as the usual  $2 \times 2$  circuitual scattering matrix for a two-port circuit [39].

The GSMs of consecutive bimaterial interfaces are linked one by one to devise a scattering matrix  $\mathcal{S}^{(n,m)}$  for the overall structure [40]. The reflectance and transmittance of the real PBG structure can be easily computed from the elements of  $\mathcal{S}^{(n,m)}$  as follows:

$$R_{nm} = \left| S_{11}^{(n,m)} \right|^2, \quad (18)$$

$$T_{nm} = \left| S_{21}^{(n,m)} \right|^2. \quad (19)$$

### 3. Numerical results and discussion

Let us now numerically analyze how the spectral locations of both Bragg and non-Bragg band gaps depend on the cross-sectional shape. We begin in Section 3.1 by analyzing ideal PBG structures with vacuum as the PPV material ( $\varepsilon_1 = \mu_1 = 1$ ), and the NPV material being non-dispersive and non-dissipative. In Section 3.2, we provide results for real PBG structures (of finite thickness and terminated on both ends by unfilled waveguide sections) wherein the NPV material is dissipative and dispersive, whereas vacuum acts as the PPV material.

#### 3.1. Ideal PBG structures

For this case, results were computed for parameters of the multilayer:  $d_1/d = 0.8$ ,  $\varepsilon_1 = \mu_1 = 1$ ,  $\varepsilon_2 = -8$ , and  $\mu_2 = -2$  implemented in (i) a parallel-plate waveguide (PPWG); (ii) a rectangular waveguide (RWG); and (iii) a circular waveguide (CWG). In order to isolate the role of the cross-sectional shape, we chose the

mode indexes  $(n, m)$  and the cross-sectional dimensional ratios such that all structures have the same cut-off wavenumber  $\Gamma_{nm}d = 0.15$ , as shown in Table 1; additionally all modes are of the  $TE$  polarization state.

Figure 2 shows the variation of the function  $L_{nm} = \cos(Kd)$  versus frequency for all six cases listed in Table 1. Inspecting this figure, it can be seen that the  $L_{nm}$  of the different waveguides and modes are superimposed. These results show that the spectral locations of the band gaps do not directly depend on the cross-sectional shape and dimensions; instead, they depend directly on the cut-off parameter, as can also be deduced from Equations (5) and (12).

It is also important to note that the passbands ( $L_{nm} \leq 1$ ) are few and very narrow. Consequently, at most frequencies, energy does not propagate through the structure. This result is due to the selection of the constitutive parameters for the PPV–NPV materials that compose the unit cell, which for most frequencies satisfy the condition of zero average index  $\bar{n} = 0$ , giving rise to an extended  $\bar{n} = 0$  band gap [18].

#### 3.2. Real PBG structure

Up to this point, the behavior of the ideal PBG structure has been analyzed for fixed cross-sectional dimensions with both constituent materials of the unit cell being non-dispersive and non-dissipative.

Table 1. Mode indexes and cross-sectional dimensional ratios such that  $\Gamma_{nm}d = 0.15$ ,  $d_1/d = 0.8$ ,  $\varepsilon_1 = \mu_1 = 1$ ,  $\varepsilon_2 = -8$ , and  $\mu_2 = -2$  for the polarization state in six different waveguides.

| Cross-sectional shape | Mode indexes   | Dimensional ratios      |
|-----------------------|----------------|-------------------------|
| Parallel-plate        | $n = 1$        | $h/d = 2.05$            |
| Parallel-plate        | $n = 2$        | $h/d = 4.1$             |
| Rectangular           | $n = 1, m = 0$ | $a/d = 2.05, b/d = 3.0$ |
| Rectangular           | $n = 2, m = 0$ | $a/d = 4.1, b/d = 3.0$  |
| Circular              | $n = 0, m = 1$ | $a/d = 2.5$             |
| Circular              | $n = 1, m = 1$ | $a/d = 1.25$            |

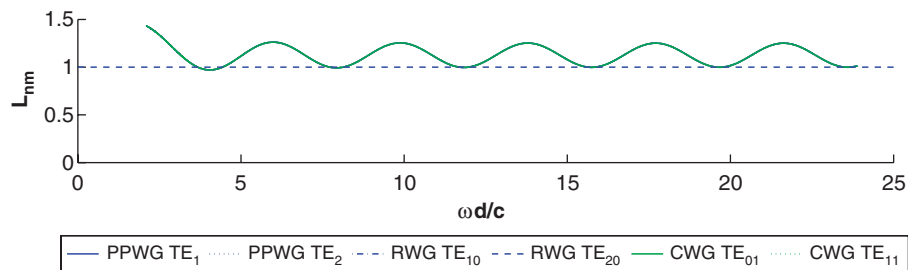


Figure 2. Variation of  $L_{nm} = \cos(Kd)$  versus  $\omega d/c$  for the waveguides and  $TE^z$  modes listed in Table 1. (The color version of this figure is included in the online version of the journal.)

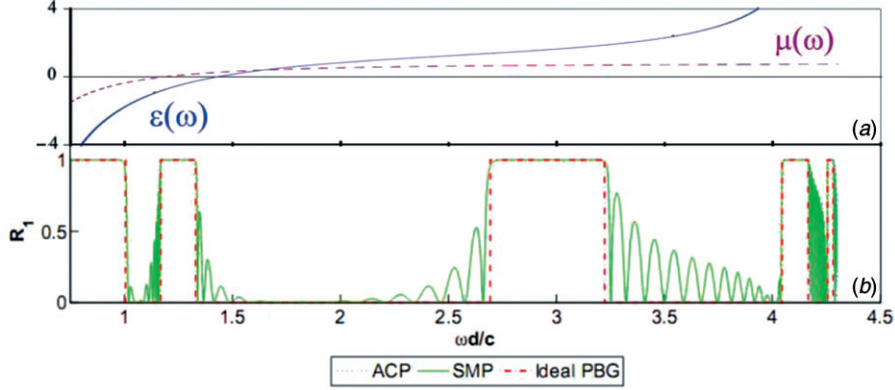


Figure 3. (a) Frequency dependence of the constitutive parameters,  $\varepsilon_2$  and  $\mu_2$ , of the NPV material; and (b) variation of reflectance versus  $\omega d/c$  for the  $TE_1^-$  mode, when a real PBG structure is implemented in a parallel-plate waveguide;  $h/d=4.5$ ,  $\varepsilon_1=\mu_1=1$ ,  $d_1/d=2/3$ ,  $\varepsilon_2$  and  $\mu_2$  are given by Equations (20) and (21) with  $\gamma=0$ , and  $N=15$ . The notional results for the corresponding ideal PBG structure  $N \rightarrow \infty$  are also presented. (The color version of this figure is included in the online version of the journal.)

In this section we study the dependence of the spectral locations of band gaps on the cross-sectional dimensions and shape of the waveguide, but with the mode index  $(n, m)$  fixed; then  $\Gamma_{nm}$  cannot be a fixed parameter. For a more general and realistic study, we also chose to consider real PBG structures wherein the NPV material is dissipative and dispersive, vacuum acts as the PPV material, the number of unit cells is finite ( $N$ ), and the waveguide is terminated on both ends with unfilled sections. As stated earlier, the Abelés–Chebyshev procedure and the scattering-matrix procedure were used.

We began by comparing the numerical results obtained by the two numerical procedures, which were also evaluated against the results obtained for an analogous ideal PBG structure. The constitutive parameters of the NPV material chosen are given by [18]

$$\varepsilon_2 = 1 + \frac{31.41^2}{5.65^2 - \omega^2 - i\gamma\omega} + \frac{62.83^2}{72.25^2 - \omega^2 - i\gamma\omega}, \quad (20)$$

$$\mu_2 = 1 + \frac{18.85^2}{5.67^2 - \omega^2 - i\gamma\omega}, \quad (21)$$

where  $\gamma$  is the damping constant. The frequency dependence of these parameters is shown in Figure 3(a): the solid line represents  $\varepsilon_2(\omega)$  and the dotted line  $\mu_2(\omega)$ .

Figure 3(b) shows the variation of the reflectance  $R_1$  versus  $\omega d/c$  for the  $TE_1^-$  mode in a real PBG structure implemented inside a parallel-plate waveguide characterized by  $h/d=4.5$ ;  $d_1/d=2/3$ ,  $N=15$ , and  $\gamma=0$ . Dotted lines indicate the results from the Abelés–Chebyshev procedure, and solid lines from the scattering-matrix procedure. In addition, the notional results for the corresponding ideal PBG structure

( $N \rightarrow \infty$ ) are presented as dashed lines. As can be seen from Figure 3(b), the results from both numerical procedures agree very well (the relative error is less than 0.01%), and the stopbands for the ideal PBG structure are located in regions where the reflectance of the real PBG structure is large. Let us also point out that the reflectance  $R_1$  in Figure 3(b) shows the presence of three different types of band gaps: the first located at  $\omega d/c \approx 0.9$  satisfies the  $\bar{n}=0$  condition (when both  $\varepsilon_2(\omega)$  and  $\mu_2(\omega)$  are negative), the second located around  $\omega d/c \approx 1.2$  corresponds to a  $\mu$ -zero gap ( $\mu_2(\omega)$  crosses from positive to negative within the gap frequency region), and finally, the rest of the band gaps are Bragg gaps.

We went on to examine the dependence of the band-gap locations on the cross-sectional dimensions and shape. Since both numerical procedures gave the same results, only results obtained with the scattering-matrix procedure method are presented.

In Figure 4, we present the variation of the reflectance  $R_{nm}$  against frequency when a real PBG structure is implemented in (a) a parallel-plate waveguide; (b) a rectangular waveguide; (c) a circular waveguide; and (d) a coaxial waveguide. In order to compare the variations, the selected modes for these gap maps are the lowest-order  $TE^z$  modes for each cross-section chosen. The plotted graphs are called ‘gap-maps’.

As observed in previous works [18,24], four types of band gaps can be identified in the gap-maps of Figure 4. The first band gap (grey zone) is due to the cut-off frequency of the input and output terminating sections. Since these waveguide sections are usually much longer than the unit cell, they control the cut-off frequency of the real PBG structure. Thus, this gap only depends on the cross-sectional

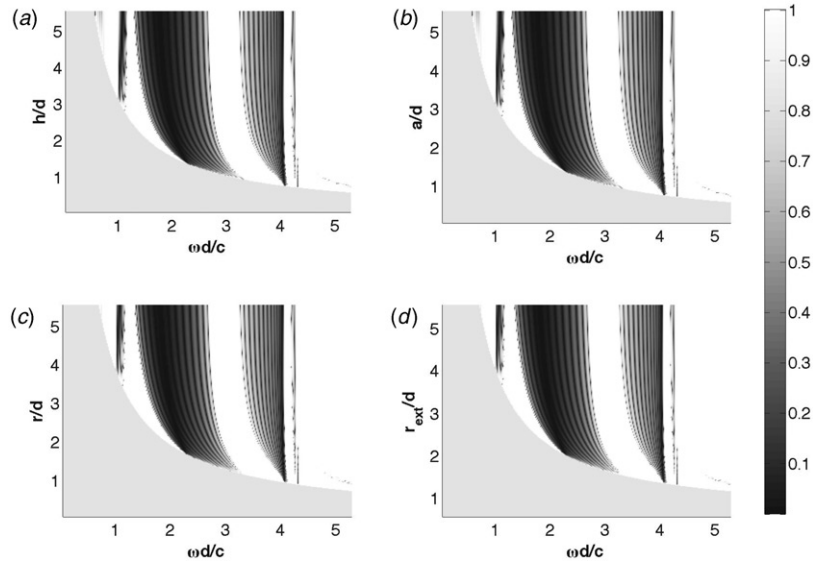


Figure 4. Variation of the reflectance versus frequency and a cross-sectional dimension of a real PBG structure implemented in: (a) a parallel-plate waveguide for the  $TE_1^z$  mode; (b) a rectangular waveguide with  $b/d=4.5$  for the  $TE_1^z$  mode; (c) a circular waveguide for the  $TE_0^z$  mode; (d) a coaxial waveguide with  $r_{in}/d=0.55$  for the  $TE_0^z$  mode. Data:  $\varepsilon_1 = \mu_1 = 1$ ,  $d_1/d=2/3$ ,  $\varepsilon_2$  and  $\mu_2$  given by Equations (20) and (21) with  $\gamma=0$ ; and  $N=15$ .

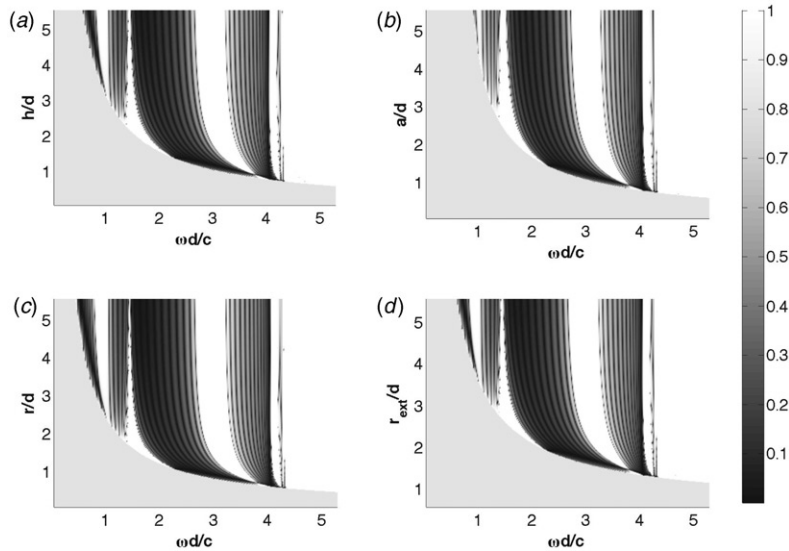
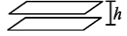
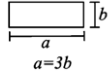
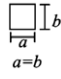
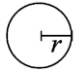



Figure 5. Variation of the reflectance versus frequency and a cross-sectional dimension of a real PBG structure implemented in: (a) a parallel-plate waveguide for the  $TM_1^z$  mode; (b) a rectangular waveguide with  $b/d=4.5$  for the  $TM_1^z$  mode; (c) a circular waveguide for the  $TM_0^z$  mode; and (d) a coaxial waveguide with  $r_{in}/d=0.55$  for the  $TM_0^z$  mode. Data:  $\varepsilon_1 = \mu_1 = 1$ ,  $d_1/d=2/3$ ,  $\varepsilon_2$  and  $\mu_2$  given by Equations (20) and (21) with  $\gamma=0$ ; and  $N=15$ .

dimensions and shape, but not on the PBG structure. The remaining band gaps are due to the PBG structure and depend on the unit cell characteristics (constitutive parameters and layer thicknesses). The second and third band gaps are not of the Bragg type: the second band gap, near  $\omega d/c=0.9$ , can be identified as a  $\bar{n}=0$  band gap, whereas the next band gap, whose width

decreases with the height for the parallel-plate and rectangular waveguides, or with the external radius (for the circular and coaxial waveguides), is the  $\mu$ -zero band gap [15]. Contrary to [23], these last two non-Bragg band gaps appear even in normal propagation due to the presence of the waveguide walls [30]. All the rest of the band gaps present in these gap-maps are

Table 2. Values of the upper and lower frequencies of band gaps for the lowest-order  $TM^z$  modes for different section geometries. (a)  $h/d=b/d=r/d=r_{\text{ext}}/d=1.5$ ; (b)  $h/d=b/d=r/d=r_{\text{ext}}/d=4.5$ . Lines represent frequencies below the cut-off frequency limit.

| $TM^z$                             |  $TM_1^z$ |  $TM_{11}^z$ |  $TM_{11}^z$ |  $TM_{01}^z$ |  $TM_{01}^z$ |       |       |
|------------------------------------|--|---|---|---|---|-------|-------|
| $h/d=b/d=r/d=r_{\text{ext}}/d=1.5$ | Bragg $\bar{n}=0$ gap  | $\omega^-d/c$   | 1.044   | —   | —   | —     |       |
|                                    |  | $\omega^+d/c$   | 1.212   | —   | —   | —     |       |
|                                    | Bragg $\varepsilon=0$ gap  | $\omega^-d/c$   | 1.358   | —   | —   | —     |       |
|                                    |  | $\omega^+d/c$   | 2.139   | 2.224   | —   | —     |       |
|                                    | Bragg gap  | $\omega^-d/c$   | 3.142   | 3.192   | 3.552   | 2.947 | 3.702 |
|                                    |  | $\omega^+d/c$   | 3.484   | 3.511   | 3.687   | 3.369 | 3.750 |
| $h/d=b/d=r/d=r_{\text{ext}}/d=4.5$ | Bragg $\bar{n}=0$ gap  | $\omega^-d/c$   | 0.884   | 0.898   | 0.995   | 0.829 | 0.907 |
|                                    |  | $\omega^+d/c$   | 1.021   | 1.024   | 1.024   | 1.019 | 1.021 |
|                                    | Bragg $\varepsilon=0$ gap  | $\omega^-d/c$   | 1.418   | 1.428   | 1.409   | 1.412 | 1.415 |
|                                    |  | $\omega^+d/c$   | 1.468   | 1.474   | 1.525   | 1.450 | 1.477 |
|                                    | Bragg gap  | $\omega^-d/c$   | 2.707   | 2.713   | 2.764   | 2.683 | 2.717 |
|                                    |  | $\omega^+d/c$   | 3.208   | 3.213   | 3.249   | 3.191 | 3.215 |

Bragg band gaps, and their origin is due to interference from the periodically repetitive constitution of the PBG structure.

In Figure 5, analogous gap-maps for lowest-order<sup>1</sup>  $TM^z$  modes are plotted. For modes of this polarization state, no  $\mu$ -zero band gap appears, but the  $\varepsilon$ -zero band gap is present instead.

The four gap-maps displayed in Figures 4 and 5 are practically the same, regardless of the cross-sectional shape. The widths of the passbands are very similar, and the small differences between the gap-maps are further reduced when the cross-sectional dimensions are slightly increased. The slight variations among the different gap-maps are due to the value the cut-off wavenumber acquires for each structure. To quantify these differences and similarities, the upper and lower frequencies of the different band gaps are compared in Table 2 and Figure 6 for the same constitutive parameters of Figures 4 and 5. These limiting frequencies were computed for the lowest-order  $TM^z$  mode for each shape, and the cross-sectional dimensions were selected for useful comparison.

In all cases, the numerical values show that the frequencies at which band-gaps occur are very similar for all the geometries, having differences at most of 10% for the worst of the comparisons. Coaxial guides differ from the other four cases by approximately 15%, because the inner diameter is not so small with respect to the outer one; this difference reduces significantly as  $r_{\text{int}} \rightarrow 0$ . In these figures, we can also distinguish the reduction of the differences between sections as relative

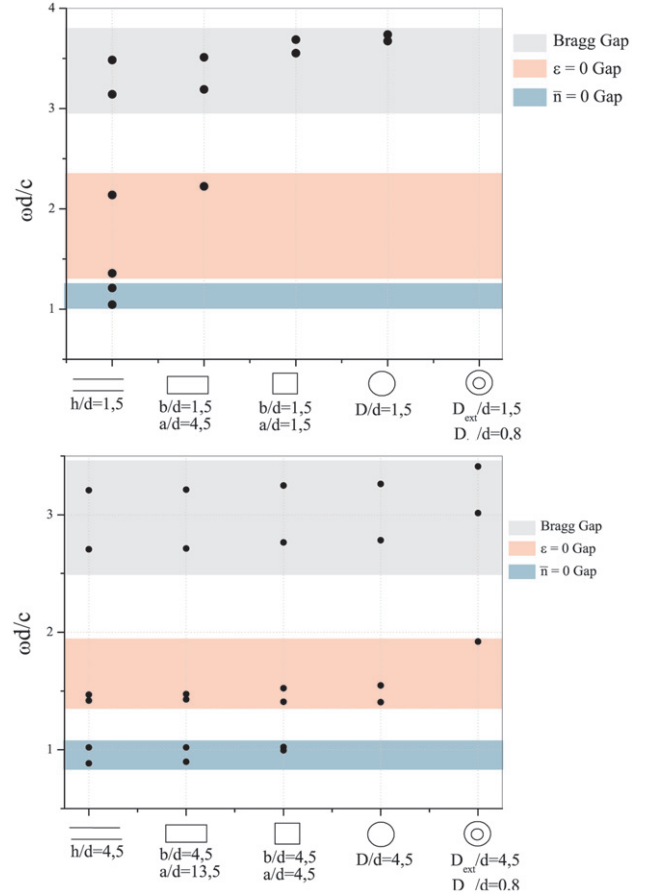


Figure 6. Schematic comparison of the frequency limits of band gaps for the lowest-order  $TM^z$  modes for the same geometries of Table 2. (The color version of this figure is included in the online version of the journal.)



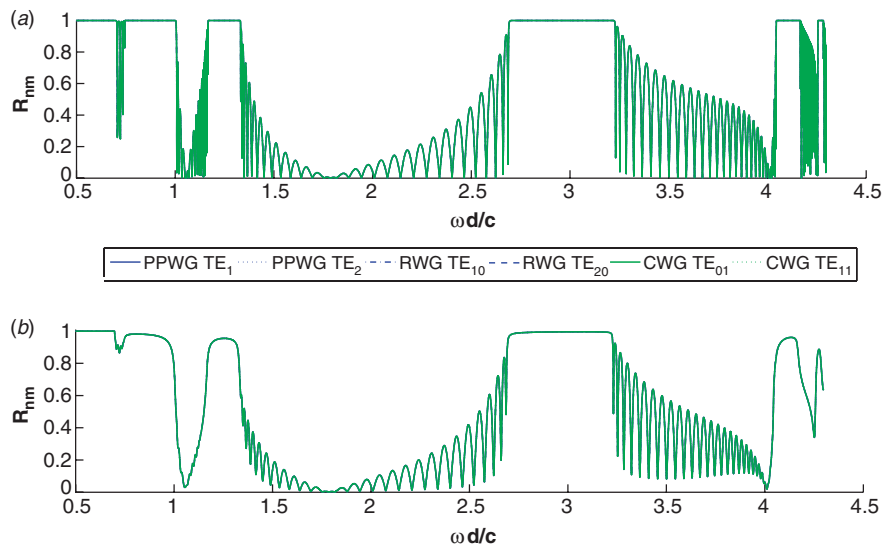


Figure 7. Reflectance spectrum of a real PBG multilayer structure implemented inside waveguides of different cross-sectional shape for diverse propagation modes. The external dimensions of each waveguide are: (i)  $h/d=4.5$  and  $h/d=9$  for, respectively,  $TM_1^z$  and  $TM_2^z$  modes of the parallel-plate waveguide; (ii)  $a/d=4.5$ ,  $b/d=9$  and  $a/d=9$ ,  $b/d=9$  for, respectively,  $TM_{10}^z$  and  $TM_{20}^z$  modes of the rectangular waveguide; (iii)  $a/d=6.49$  and  $a/d=2.64$  for, respectively,  $TE_{01}^z$  and  $TE_{11}^z$  modes of the circular waveguide. Also,  $\varepsilon_1 = \mu_1 = 1$ ,  $d_1/d = 2/3$ ,  $\varepsilon_2$  and  $\mu_2$  are given by Equations (20) and (21) with (a)  $\gamma=0$  and (b)  $\gamma=0.16$ , and  $N=30$ . (The color version of this figure is included in the online version of the journal.)

distances enlarge. Lines or absent points in Table 2 and Figure 6, respectively, represent frequencies below the cut-off frequency ( $\Gamma_{nm}$ ).

Finally, we plot in Figure 7 the reflectance spectrum of a real PBG multilayer structure with  $N=30$  unit-cells implemented inside the different cross-sectional shaped waveguides considered in the previous figures. The external dimensions of the diverse waveguides are fixed in order to obtain the same cut-off wavenumber for the chosen propagation modes. Results are shown for both non-dissipative ( $\gamma=0$ ) and dissipative ( $\gamma=0.16$ ) NPV materials, exhibiting that the reflectance spectrum of each structure yields band gaps located in the same frequency range.

#### 4. Conclusions

We have studied here the responses of PBG structures that alternate conventional dielectrics with negative phase velocity materials implemented in waveguides of different cross-sections. Our results show that the reflectance spectrum does not depend directly on the cross-sectional geometry but on the cut-off wavenumber instead. Therefore, only the cross-sectional dimensions that control the cut-off wavenumber are capable of modifying the spectral localization of the band gaps when the unit-cell parameters (constitutive parameters and widths of layers) are fixed. Results obtained using two alternative numerical methods, the Abelés–Chebyshev and the Scattering Matrix

procedures, show that structures exhibit both Bragg and non-Bragg gaps even for normal propagation. Simulations with lossy materials have been included showing that the spectral localization of the band gaps remains invariant for low loss.

#### Acknowledgements

Álvaro Gómez was supported by the Dirección General de Investigación of the Spanish Ministerio de Educación y Ciencia, under the project/grant TEC2006–13268–C03–01. Akhlesh Lakhtakia thanks the Charles Godfrey Binder Endowment at Penn State for partial support. Maria Luz Martínez Ricci and Ricardo Depine acknowledge financial support from Consejo Nacional de Investigaciones Científicas y Técnicas (CONICET), Agencia Nacional de Promoción Científica y Tecnológica (PID1728/OC–AR PICT-11–1785) and Universidad de Buenos Aires (UBA–X062).

#### Note

1. The  $TM_0^z$ , i.e. the  $TEM$  mode is not taken in account for the parallel-plate waveguide. Therefore, the  $TM_1^z$  is the lowest-order  $TM^z$  mode.

#### References

- [1] Joannopoulos, J.D.; Johnson, S.G.; Winn, J.N.; Meade, R.D. *Photonic Crystals: Molding the Flow of Light*, 2nd ed.; Princeton University Press: Princeton, NJ, USA, 2008.

- [2] Felbacq, D.; Zolla, F. Scattering theory of periodic crystals. In *Introduction to Complex Mediums for Optics and Electromagnetics*; Weiglhofer, W.S., Lakhtakia, A., Eds.; SPIE Press: Bellingham, WA, USA, 2003; pp 365–393.
- [3] Haus, J.W. Photonic band gap structures. In *Nanometer Structures: Theory, Modeling and Simulation*; Lakhtakia, A., Ed.; SPIE Press: Bellingham, WA, USA, 2004; pp 45–106.
- [4] Russel, P.St.J.; Tredwell, S.; Roberts, P.J. *Opt. Commun.* **1990**, *160*, 66–71.
- [5] Chigrin, D.N.; Lavrinenko, A.V.; Yarotsky, D.A.; Gaponenko, S.V. *Appl. Phys. A* **1999**, *68*, 25–28.
- [6] Lodahl, P.; Floris van Driel, A.; Nikolaev, I.S.; Irman, A.; Overgaag, K.; Vanmaackelbergh, D.; Vos, W.L. *Nature* **2004**, *430*, 654–657.
- [7] Baumeister, P.W. *Optical Coating Technology*; SPIE Press: Bellingham, WA, USA, 2004.
- [8] Srivastava, S.K.; Ojha, S.P.; Ramesh, K.S. *Microw. Opt. Technol. Lett.* **2002**, *33*, 308–314.
- [9] Gómez, A.; Solano, M.A.; Lakhtakia, A.; Vegas, A. *Proc. SPIE* **2003**, *5218*, 191–200.
- [10] Veselago, V.G. *Soviet Phys. Usp.* **1968**, *10*, 509–514, [*Usp. Fiz. Nauk.* **1967**, *92*, 517–526].
- [11] Shelby, R.A.; Smith, D.R.; Schultz, S. *Science* **2001**, *292*, 77–79.
- [12] Caloz, C.; Itoh, T. *Electromagnetic Metamaterials: Transmission Line Theory and Microwave Applications*; Wiley: Hoboken, NJ, USA, 2006.
- [13] Wood, B. *Laser Photon. Rev.* **2007**, *1*, 249–259.
- [14] Depine, R.A.; Lakhtakia, A. *Microw. Opt. Technol. Lett.* **2004**, *41*, 315–317.
- [15] Lakhtakia, A.; McCall, M.W.; Weiglhofer, W.S. *AEÜ Int. J. Electron. Commun.* **2002**, *56*, 407–410.
- [16] Pendry, J.B. *Phys. Rev. Lett.* **2000**, *85*, 3966–3969.
- [17] Wu, L.; He, S.; Shen, L. *Phys. Rev. B* **2003**, *67*, 235103.
- [18] Li, J.; Zhou, L.; Chan, C.T.; Sheng, P. *Phys. Rev. Lett.* **2003**, *90*, 083901.
- [19] Ruppin, R. *Microw. Opt. Technol. Lett.* **2003**, *38*, 494–495.
- [20] Lakhtakia, A. *Int. J. Infrared Millim. Waves* **2002**, *23*, 339–343.
- [21] Ramm, A. *Phys. Lett. A* **2008**, *372*, 6518–6520.
- [22] D’Aguanno, G.; Mattiucci, N.; Bloemer, M.J. *J. Opt. Soc. Am. B* **2008**, *25*, 236–246.
- [23] Depine, R.A.; Martínez-Ricci, M.L.; Monsoriu, J.A.; Silvestre, E.; Andrés, P. *Phys. Lett. A* **2007**, *364*, 352–355.
- [24] Monsoriu, J.A.; Depine, R.A.; Martínez-Ricci, M.L.; Silvestre, E. *Opt. Express* **2006**, *14*, 12958–12967.
- [25] Dolling, G.; Wegener, M.; Soukoulis, C.M.; Linden, S. *Opt. Lett.* **2007**, *32*, 53–55.
- [26] Liu, N.; Guo, H.; Fu, L.; Kaiser, S.; Schweizer, H.; Giessen, H. *Nature Mater.* **2008**, *7*, 31–37.
- [27] Jen, Y.-J.; Lakhtakia, A.; Yu, C.-W.; Lin, C.-T. *Opt. Express* **2009**, *17*, 7784–7789.
- [28] Peacock, A.C.; Broderick, N.G.R. *Opt. Express* **2003**, *11*, 2502–2510.
- [29] Shadrivov, I.V.; Sukhorukov, A.A.; Kivshar, Y.S. *Phys. Rev. E* **2003**, *67*, 057602.
- [30] Depine, R.A.; Martínez-Ricci, M.L.; Lakhtakia, A. *Microw. Opt. Technol. Lett.* **2006**, *48*, 2365–2372.
- [31] Collin, R.E. *Field Theory of Guided Waves*, 2nd ed.; IEEE Press: Piscataway, NJ, USA, 1991; Chapter 5.
- [32] Jackson, J.D. *Classical Electrodynamics*, 3rd ed.; Wiley: New York, USA, 1999; Chapter 8.
- [33] Kittel, C. *Introduction to Solid State Physics*, 4th ed.; Wiley Eastern: New Delhi, India, 1971.
- [34] Gómez, A.; Lakhtakia, A.; Solano, M.A.; Vegas, A. *Microw. Opt. Technol. Lett.* **2003**, *38*, 511–514.
- [35] Solano, M.A.; Gómez, A.; Lakhtakia, A.; Vegas, A. *Int. J. Electron.* **2005**, *92*, 117–130.
- [36] Gómez, A.; Solano, M.A.; Lakhtakia, A.; Vegas, A. *Microw. Opt. Technol. Lett.* **2003**, *37*, 316–321.
- [37] Abelés, F. *Ann. Phys. (Paris)* **1950**, *5*, 596–640.
- [38] Griffiths, D.J.; Steinke, C.A. *Am. J. Phys.* **2001**, *69*, 137–154.
- [39] Collin, R.E. *Foundations for Microwave Engineering*, 2nd ed.; McGraw-Hill: New York, 1992; Chapter 4.
- [40] Van Blaricum, G.F.; Mittra, R. *IEEE Trans. Microwave Theory Tech.* **1969**, *17*, 310–319.